nature photonics

ARTICLES

PUBLISHED ONLINE: 4 MARCH 2012 | DOI: 10.1038/NPHOTON.2012.27

# A comparison of graphene, superconductors and metals as conductors for metamaterials and plasmonics

Philippe Tassin[1]*, Thomas Koschny[1], Maria Kafesaki[2] and Costas M. Soukoulis[1,2]

**Recent advancements in metamaterials and plasmonics have promised a number of exciting applications, in particular at terahertz and optical frequencies. Unfortunately, the noble metals used in these photonic structures are not particularly good conductors at high frequencies, resulting in significant dissipative loss. Here, we address the question of what is a good conductor for metamaterials and plasmonics. For resonant metamaterials, we develop a figure-of-merit for conductors that allows for a straightforward classification of conducting materials according to the resulting dissipative loss in the metamaterial. Application of our method predicts that graphene and high-$T_c$ superconductors are not viable alternatives for metals in metamaterials. We also provide an overview of a number of transition metals, alkali metals and transparent conducting oxides. For plasmonic systems, we predict that graphene and high-$T_c$ superconductors cannot outperform gold as a platform for surface plasmon polaritons, because graphene has a smaller propagation length-to-wavelength ratio.**

Metamaterials and plasmonics, two branches of the study of light in electromagnetic structures, have emerged as promising scientific fields. Metamaterials are engineered materials that consist of subwavelength electric circuits replacing atoms as the basic unit of interaction with electromagnetic radiation[1–3]. They can provide optical properties beyond those achievable in natural materials, such as magnetism at terahertz and optical frequencies[4–6], negative index of refraction[7–9] or giant chirality[10]. Plasmonics exploits the mass inertia of electrons to create propagating charge density waves at the surface of metals[11,12], which may be useful for intrachip signal transmission, biophotonic sensing applications and solar cells, among others[13–15].

Unfortunately, although metamaterials and plasmonic systems promise the harnessing of light in unprecedented ways, they are also plagued by dissipative losses—probably the most important challenge to their applicability in real-world devices. In metamaterials, this results in absorption coefficients of tens of decibels per wavelength in the optical domain[16]. In plasmonic systems, dissipative loss is reflected in the limited propagation length of surface plasmon polaritons (SPPs) on the surface of noble metals[17,18]. These losses originate in the large electric currents, leading to significant dissipation in the form of Joule heating, and enhanced electromagnetic fields close to the metallic constituents, leading to relaxation losses in the dielectric substrates on which the metallic elements are deposited. It must be borne in mind that even if the loss tangent of the constituent materials is small, significant losses still occur because the loss channels are driven by large resonant fields. Focusing on terahertz frequencies and higher, loss is dominated by dissipation in the conducting elements, even if noble metals with relatively good electrical properties (for example, silver or gold) are used.

It has been proposed to reduce the loss problem by replacing noble metals by other material systems[19], such as graphene[20,21] or high-temperature superconductors[22]. Both material systems are known to be good conductors, at least for direct currents, and merit further investigation for use in metamaterials or plasmonic systems.

In this work, we answer the question of what is a good conductor for use in metamaterials and in plasmonics. Should it have small or large conductance? Does the imaginary part of the conductivity (or real part of the permittivity, for that matter) improve or worsen the loss? Different applications, for example, long-range surface plasmons or metamaterials with negative permeability, require conductors with different properties. For resonant metamaterials we derive a figure-of-merit measuring the dissipative loss that contains the properties of the conducting material—the resistivity—and certain geometric aspects of the conducting element. We apply this figure-of-merit to compare graphene, high-$T_c$ superconductors, transparent conducting oxides, transition and alkali metals, and some metal alloys. For plasmonics systems, we use the ratio of the propagation length to the surface plasmon wavelength as the measure of loss performance, and we evaluate graphene as a platform for surface plasmons.

## A figure-of-merit for conductors in resonant metamaterials

The metamaterials we consider here consist of an array of subwavelength conducting elements; it is for this type of structure that an effective permittivity and permeability makes sense[23–26]. This allows modelling each individual element as a quasistatic electrical circuit described by an RLC circuit. This is not the most general case, as some reported phenomena in metamaterials require more intricate circuits[27–30], but it has been proven that it can capture effectively the physics of the most popular elements, such as split rings and wire pairs[31].

Our analysis starts with describing the electrical current flowing in the metallic circuit of each meta-atom. Subsequently, we calculate the permeability of the metamaterial and the dissipated power by summing the Joule heat loss for each circuit[32] (see Methods for a detailed derivation). Expressed in dimensionless quantities, we

[1]Ames Laboratory—US DOE and Department of Physics and Astronomy, Iowa State University, Ames, Iowa 50011, USA, [2]Institute of Electronic Structure and Lasers (IESL), FORTH, 71110 Heraklion, Crete, Greece. *e-mail: tassin@ameslab.gov

find that the dissipated power as a fraction of the incident power can be cast in the following form:

$$\Pi = \frac{\text{dissipated power per unit cell}}{\text{incident power per unit cell}} = 2\pi\left(\frac{a_k}{\lambda_0}\right)\frac{F\tilde{\omega}^4\zeta}{\left[\tilde{\omega}^2(1+\xi)-1\right]^2+\left(\tilde{\omega}\zeta+\tau\tilde{\omega}^5\right)^2} \quad (1)$$

where $\tilde{\omega} = \omega/\omega_0$ is the renormalized frequency, with $\omega_0 = (LC)^{-1/2}$ being the resonance frequency of the quasistatic circuit, $F$ is the filling factor of the metal in the unit cell, $\zeta = \mathrm{Re}(R)/\sqrt{(L/C)}$ is the dissipation factor, $\xi = -\mathrm{Im}(R)/(\tilde{\omega}\sqrt{(L/C)})$ is the kinetic inductance factor, and $\tau$ is a parameter describing radiation loss. $a_k$ is the unit cell size of the metamaterial along the propagation direction and $\lambda_0$ is the free-space wavelength. We will discuss the physical significance of these parameters in the following.

It is interesting to note that the dissipated power fraction quantifying the dissipative loss depends on just four independent, dimensionless parameters: (i) the filling factor, $F$; (ii) the radiation loss parameter, $\tau$; (iii) the dissipation factor, $\zeta$ (proportional to the real part of the resistivity); and (iv) the kinetic inductance factor, $\xi$ (proportional to the imaginary part of the resistivity). The filling factor and the radiation loss parameter depend only on purely geometric variables, such as the area of the circuit and the geometric inductance, but not on the material properties of the conductor. So, for a certain geometry (say, split rings or fishnet), $F$ and $\tau$ are fixed. This means we can limit this study to how the dissipated power depends on $\zeta$ and $\xi$, the only two parameters that depend on the specific conducting material used. Figure 1a presents a contour plot of the dissipated power fraction as a function of these two parameters. As our aim is to design metamaterials with negative permeability ($\mu$), we calculated the dissipated power at the frequency where $\mu(\omega) = -1$. Apart from the uninteresting regions with very high dissipation factor and/or kinetic inductance factor (top and rightmost regions), we see that the contours of equal dissipated power are almost vertical; that is, the dissipative loss depends, to a good approximation, only on the dissipation factor. We can therefore replot the dissipated power fraction as a function of the dissipation factor (Fig. 1c). The different blue curves in this figure represent the dissipated power fraction for several values of achieved permeability. We observe that smaller $\zeta$ (that is, smaller real part of the resistivity) leads to lower power dissipation, even though smaller resistivity implies quasistatic circuits with sharper resonances.

This behaviour can be understood from examining Fig. 1b. For large dissipation factors (metamaterials made from high-resistivity materials), the resonance is highly damped; the peak loss at the resonance frequency is relatively low and the resonance is too shallow to allow for permeability $\mu = -1$. With decreasing dissipation factor, the resonance becomes sharper; the dissipated power at the resonance frequency increases (red curve in Fig. 1c), but for a given design goal of the permeability (for example, $\mu = -1$), the resonance may be probed farther from the resonance peak, effectively leading to smaller dissipated power. When the dissipation factor is further decreased, the linewidth becomes limited by the radiation loss, which implies that the current in the circuit does not further increase. From this point on, the resonance does not become any stronger when the dissipation factor is further decreased (that is, when a better conductor is used). Therefore, one cannot achieve arbitrarily low permeability, but, on the contrary, there is a geometrical limit on the strongest negative permeability that can be achieved with a certain structure. As the induced current in the circuit now becomes constant when further decreasing the dissipation factor, the dissipated power at the working frequency continues to decrease linearly with the dissipation factor, because the Joule heating is proportional to the resistivity.

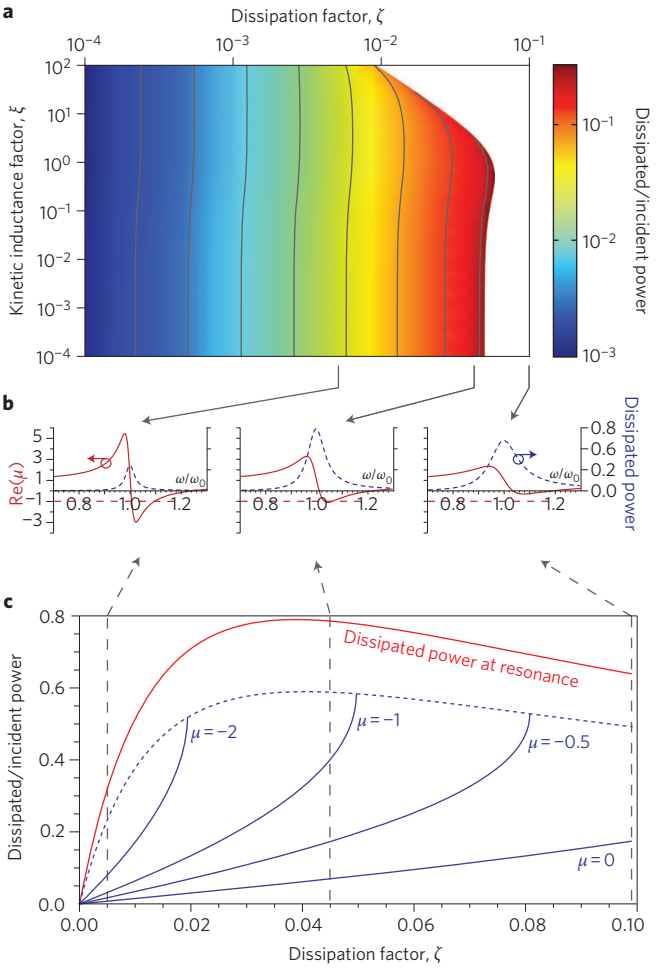


**Figure 1 | Dissipated power in a metamaterial with $F = 0.37$ and $\tau = 0.039$ (quantities calculated for the slab-wire pair of Fig. 2a).** **a**, Contour plot of dissipated power (calculated at the operating frequency where $\mu(\omega) = -1$) as a function of dissipation factor $\zeta$ and kinetic inductance factor $\xi$. Apart from the uninteresting region of high dissipation/high kinetic inductance, the contours are vertical, indicating that the dissipated power depends, to a good approximation, only on the dissipation factor. **b**, Resonance shapes of the magnetic permeability (red lines) and the dissipated power (blue dashed lines) for different dissipation factors. **c**, Dissipated power as a function of the dissipation factor. The red line indicates the peak dissipative loss at the resonance frequency. Blue lines represent the dissipative loss at constant permeability. The dashed blue line indicates the cutoff; for higher dissipation factors the desired permeability can no longer be achieved.

In a similar way, we can show that the kinetic inductance factor determines frequency saturation due to the kinetic inductance[31,33] (see Supplementary Information).

In summary, the dissipative loss in resonant metamaterials can be determined from a single dimensionless parameter—the dissipation factor. From Fig. 1c, it can be observed that the dissipated power is a monotonic function of the dissipation factor, even approaching a linear function for small $\zeta$. This unambiguously establishes the dissipation factor $\zeta$ as a good figure-of-merit for conducting materials in resonant metamaterials. Whenever a new conducting material is proposed, the dissipation factor allows for a quick and straightforward assessment of the merits of this conducting material for use in the current-carrying elements of resonant metamaterials.

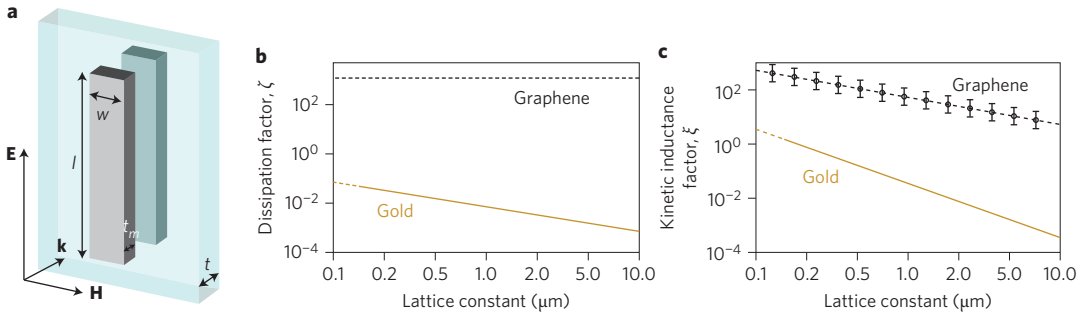


**Figure 2 | Comparison between the loss factors and kinetic inductance factors of charge-neutral graphene and gold. a**, The slab-wire pair used as an example of a magnetic metamaterial (parameters provided in Methods). **b**, Dissipation factors for the slab-wire pair made from graphene and from gold. **c**, Kinetic inductance factors for the slab-wire pair made from graphene and from gold. (The full lines indicate that the structure can provide negative permeability ($\mu = -1$); the dashed lines indicate that the structure is beyond the cutoff and the resonance is too shallow to obtain $\mu = -1$.).

We conclude that resonant metamaterials benefit from conducting materials with smaller real part of the resistivity. However, when comparing conducting materials for which samples of comparable thickness cannot be fabricated, the geometrical details in the dissipation factor become important. This will be essential when we investigate the two-dimensional conductor graphene in the next section. Note that we have derived the loss factor for negative-permeability metamaterials, but it is also applicable to other metamaterials that rely on the resonant response of other polarizabilities, for example, with negative permittivity and giant chirality.

## Graphene at optical frequencies

Graphene is a two-dimensional system in which electric current is carried by massless quasiparticles[34,35]. We have seen above that for low-loss resonant metamaterials, we need conducting materials with a small real part of the resistivity (to allow for large currents) and small imaginary part of the resistivity (to avoid saturation of the resonance frequency). Band structure calculations and recent experiments indicate that minimal resistivity in the mid-infrared and visible band is achieved for charge-neutral graphene, where the surface conductivity equals the universal value $\sigma_0 = \pi e^2/2h$ (refs 36–38).

For the slab-wire pair of Fig. 2a, we have calculated the dissipation factor (Fig. 2b) and the kinetic inductance factor (Fig. 2c) for gold and graphene. Gold slab-wire pairs can provide negative permeability ($\mu = -1$) if the lattice constant is larger than 0.15 μm (full line). For smaller lattice constants (dashed line), the dissipation factor increases above the cutoff at which negative permeability cannot be achieved. The dissipation and kinetic inductance factors for graphene are several orders of magnitude larger than for gold. The dissipation factor of graphene is 1,200, which is deep into the cutoff region of Fig. 1a, where the losses are tremendous and the magnetic resonance is highly damped. In addition, the dissipation factor of graphene is scale-invariant; graphene cannot be made a better conductor by making the slab-wire pair larger. We must conclude that graphene is not conducting well enough for use in resonant metamaterials at infrared and visible frequencies.

This observation might not be so surprising given that recent results have demonstrated the optical transmittance through a free-standing graphene sheet to be more than 97%; that is, graphene has a fairly small interaction cross-section with optical radiation[38]. Many works have ascribed a high bulk conductivity to graphene—obtained by dividing its surface conductivity by the 'thickness' of the monatomic layer. This is true, but irrelevant for metamaterial purposes, where it is the total transported current that is important. However, graphene might still be useful for metamaterials when it is combined with a metallic structure[39].

There has been recent interest in using graphene as a platform for SPPs[20,21,40,41]. For plasmonics, it is desirable to work with biased graphene, because it has much larger kinetic inductance [Im($\sigma$)] than charge-neutral graphene. From Supplementary Fig. 4a, we see that biased graphene indeed supports SPPs with wavelengths much smaller than the free-space wavelength. At 30 THz, for example, the wavelength of SPPs is 0.2 μm. Graphene may thus allow for the manipulation of surface plasmons on a micrometre scale at infrared frequencies. In addition, these SPPs are excellently confined to the graphene surface with submicrometre lateral decay lengths (Supplementary Fig. 4b).

To minimize the loss, we can work in the frequency window just below the threshold of interband transitions where the Drude response of the free electrons is small and the interband transitions are forbidden due to Pauli blocking. The effect of dissipation on SPPs can be best measured by the ratio of their propagation length and wavelength. Figure 3 plots this ratio for gold (yellow curve) and graphene (black curve), calculated from experimental conductivity data obtained by Li *et al.*[36]. The propagation length is at best of the order of one SPP wavelength for strongly biased graphene in the infrared. One might object that cleaner graphene samples with smaller Re($\sigma$) might be fabricated in the future. Therefore, as a best-case scenario for SPPs on graphene, we also determined the SPP propagation length based on theoretical data for clean graphene taking into account electron–electron interactions[42,43], which fundamentally limit the conductivity of graphene. We find slightly improved propagation lengths (red curve), but not larger than three SPP wavelengths.

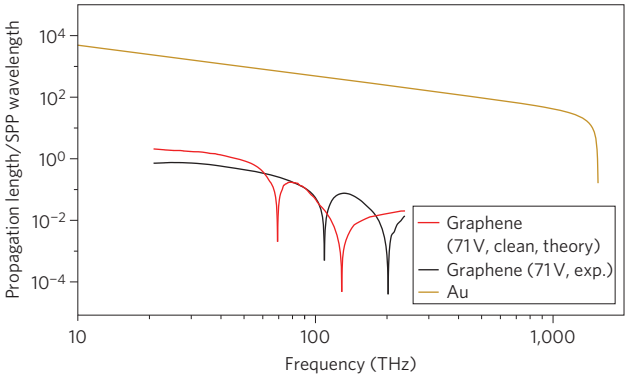


**Figure 3 | Comparison of the plasmonic properties of graphene and gold.** The results for gold are for a 30-nm-thick film at room temperature. The results for graphene are for strongly biased graphene calculated from experimental (exp.) conductivity data (from ref. 36) and calculated from theoretical conductivity data that incorporates electron–electron interactions (from ref. 42). Calculations based on theoretical data for the conductivity of graphene serve as a best-case scenario, because electron–electron interactions are an intrinsic effect.

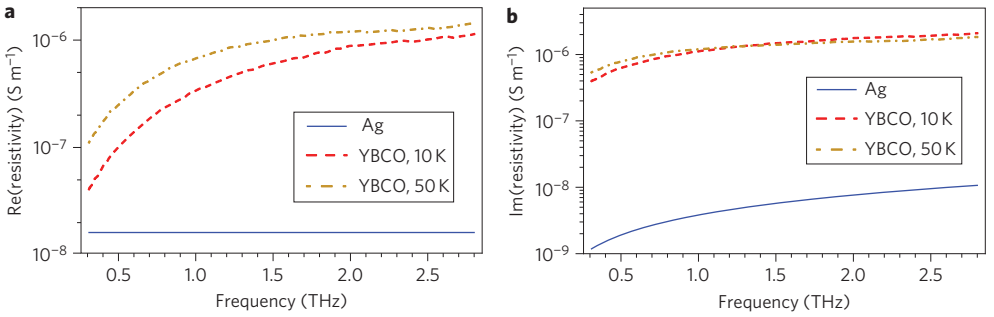


**Figure 4 | Comparison of the superconductor YBCO at 10 and 50 K (below the critical temperature of 80 K) with silver at room temperature. a**, Real part of the resistivity as a measure of the dissipative loss. **b**, Imaginary part of the resistivity as a measure of kinetic inductance.

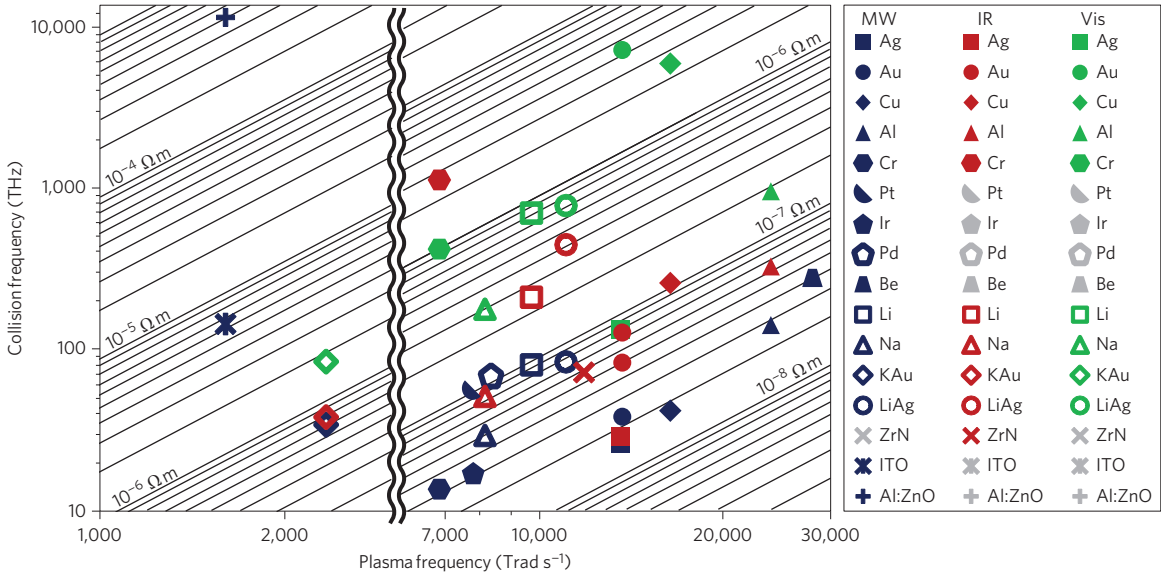


**Figure 5 | Overview of conducting materials classified according to their plasma frequency and collision frequency.** The different symbols indicate different materials (see key). The collision frequency takes into account all scattering from the conducting electronic states (electron–phonon scattering, interband transitions and so on) and therefore depends upon frequency. Blue symbols indicate material properties at microwave (MW) frequencies, red symbols in the infrared (IR, 1.55 μm), and green symbols in the visible (Vis, 500 nm). Oblique lines indicate a constant real part of the resistivity and therefore equal loss performance in metamaterials according to our analysis.

Such short propagation lengths will probably be detrimental to most plasmonic applications.

## High-temperature superconductors at terahertz frequencies

A successful approach towards low-loss microwave metamaterials is the use of type-I superconductors[44]. The microwave resistivity (5 GHz) of niobium sputtered films, for example, is $1.6 \times 10^{-13}\Omega$m at 5 K, roughly five orders of magnitude smaller than silver. Unfortunately, this approach is rendered ineffective at terahertz frequencies, because terahertz photons have sufficient energy to break up the Cooper pairs that underlie the superconducting current transport. It has therefore been suggested to use high-temperature superconductors with a larger bandgap.

We know from the above analysis that we must compare the resistivity, which is the geometry-independent part of the dissipation factor (we can leave out the geometrical terms here because metallic and superconducting films of the same thickness can be fabricated). Figure 4 presents a comparison of silver (data from ref. 45) and yttrium barium copper oxide (YBCO; data from ref. 46). We observe that from 0.5 THz to 2.5 THz, both the real part of the resistivity (dissipation) and the imaginary part (kinetic inductance) of YBCO are significantly larger than those of silver. We therefore conclude that high-$T_c$ superconductors do not perform better than silver as conducting materials at terahertz frequencies. The reason for the high resistivity values of YBCO is the specific current transport process occurring in a superconductor. For direct current (d.c.), the electrons in the normal state are completely screened by the superfluid—hence its zero d.c. resistivity. At non-zero frequencies, however, the screening is incomplete because of the finite mass of the Cooper pairs. The lossy electrons in the normal state therefore contribute to the conductance. Also, in type-II superconductors, the superfluid has loss mechanisms of its own, like flux creep. Both effects lead to a non-zero resistivity, even at frequencies well below the bandgap of the superconductor[44].

For the sake of completeness, we mention that the plasma frequencies of superconductors are not much larger than those of gold; in other words, they have similar kinetic inductance. So, at frequencies below the bandgap of the superconductor, the dispersion relation of surface plasmons is very close to the light line and superconductors do not support well-confined SPPs.

## Comparative study of metals and conducting oxides

In Fig. 5, we have classified a variety of conducting materials according to their plasma frequency and collision frequency. The collision frequency takes into account all scattering from the conducting electronic states (electron–phonon scattering, interband

transitions and so on) and therefore depends on frequency. For most materials, the conductivity in the microwave band (blue symbols in Fig. 5) is dominated by electron–phonon scattering, although interband transitions may already contribute significantly. At higher frequencies, in the infrared band (red symbols) and the visible band (green symbols), the interband transition scattering becomes larger, in particular close to frequencies matching a transition with high density of states.

At microwave frequencies (blue symbols in Fig. 5), silver and copper have the smallest resistivity; copper is frequently used for its excellent compatibility with microwave technology. Transition metals such as gold, aluminium, chromium and iridium still perform well. The dissipation factors obtained at microwave frequencies are very small and losses in the metals are typically modest (in fact the main loss channel is relaxation losses in the dielectric substrates). In the infrared (red symbols), the resistivity of copper is increased by a factor of ten due to interband transitions at 560 nm. The dissipation factors at infrared frequencies are much higher not only due to higher resistivity, but also due to the geometrical scaling of the dissipation factor as shown in Fig. 2b. Gold performs better than copper in the infrared and is easy to handle experimentally. The reader might notice we have two data points in Fig. 5 for gold at 1.55 μm; we believe this disparity originates from different grain sizes, which emphasizes the importance of sample preparation. The best conducting material with the lowest resistivity now becomes silver, due to its lowest interband transitions being in the ultraviolet (308 nm). We found that ZrN performs similarly to gold. When further scaling down metamaterials for operation in the visible (green symbols), the resistivity of most of the abovementioned metals becomes prohibitively high[47] and dissipative losses become too high to obtain, for example, negative permeability. The only reasonably performing metal in the visible is silver.

Finding new materials with smaller optical resistivity could have an important impact on the field of metamaterials. We therefore analysed a number of recently proposed alternative conducting materials, for example, transparent conducting oxides such as indium tin oxide and Al:ZnO. We find they have a microwave resistivity (blue symbols, Fig. 5) already two or more orders of magnitude larger than the optical resistivity of silver. Thus, we can rule out these materials—just as for graphene (analysed above), they interact too weakly with light. Alkali metals suffer less from interband transitions (compare in Fig. 5 the change in collision frequency from blue → red → green for lithium/sodium versus copper). Unfortunately, their intraband collision frequency is significantly larger and they tend to have a smaller plasma frequency, increasing the average energy lost in each collision. There has also been recent interest in alkali–noble intermetallics with the motivation of combining the low intraband resistivity of the noble metals with the reduced interband transition contribution of the alkali metals[48]. Two characteristic examples are KAu and LiAg. KAu (open diamond symbols in Fig. 5) has its interband transitions far in the ultraviolet and its resistivity increases only slightly from the microwave through the visible; however, its small plasma frequency leads to a relatively large resistivity. On the other hand, LiAg (open circles in Fig. 5) has a larger plasma frequency, but performs badly at higher frequencies because of significant interband scattering. These examples show, nevertheless, the possibility of band engineering to tune the resistivity of alloys[49]. We believe it is worth continuing the research effort to develop better conducting materials, because of the considerable improvement such materials would bring.

## Methods

The comparative study of conducting materials for resonant metamaterials presented in this work is based on the fact that the dissipative loss in normalized units can be written as a function of two material-dependent parameters—the dissipation factor and the kinetic inductance factor—as expressed in equation (1). This equation is obtained from a quasistatic analysis assuming the conductive elements of the metamaterial to be smaller than the free-space wavelength of the incident radiation. Special attention was paid to the radiation resistance, as its neglect would lead to a circuit model where the dissipated power could become larger than the incident power. The radiation resistance term is obtained from a near-field expansion of the magnetic fields generated by the circuit current, which is again justified by the subwavelength dimensions of the circuit. The details of the derivation of equation (1) are given in the Supplementary Methods and Supplementary Fig. 1.

Throughout the manuscript, we exemplified the classification procedure for conducting materials using a particular metamaterial constituent—the slab-wire pair. Nevertheless, the same procedure is applicable for any other metamaterial consisting of subwavelength conducting elements. The slab-wire pair (shown in Fig. 2a) had dimensions of $l = 2.19a_k$, $w = 0.47a_k$, $t = 0.5a_k$, $t_m = 0.25a_k$ ($t_m$ is of course not relevant for two-dimensional conductors such as graphene), $a_E = 2.97a_k$ and $a_H = 2.19a_k$. The relative permittivity of the substrate was $\varepsilon_r = 2.14$.

We used simple expressions for the parallel-plate capacitor and the solenoid inductance, which were shown to provide an adequate description for the slab-wire pair[31]:

$$C = \varepsilon_0\varepsilon_r\frac{wl}{t}, \quad L = \mu_0\frac{lt}{a_H}, \quad R = \frac{\rho}{t_m}\frac{2l}{w} \tag{2}$$

The area enclosed by the circuit is

$$A = lt \tag{3}$$

This is sufficient to calculate the geometry-dependent term of the dissipation and kinetic inductance factors,

$$\begin{aligned}\zeta &= \frac{\mathrm{Re}(\rho)}{t_m}\sqrt{\frac{\varepsilon_0}{\mu_0}}\sqrt{\varepsilon_r}\frac{2l\sqrt{a_H}}{t\sqrt{w}}\\ \xi &= \frac{\mathrm{Im}(\rho)}{t_m}\frac{1}{\tilde{\omega}}\sqrt{\frac{\varepsilon_0}{\mu_0}}\sqrt{\varepsilon_r}\frac{2l\sqrt{a_H}}{t\sqrt{w}}\end{aligned} \tag{4}$$

The filling factor $F$ and the radiation loss parameter $\tau$ can also be calculated:

$$\begin{aligned}F &= \mu_0A^2N/L = \frac{lt}{a_ka_E} = 0.37\\ \tau &= \frac{1}{6\pi}\frac{\sqrt{\mu_0/\varepsilon_0}}{\sqrt{L/C}}\frac{\omega_0^4A^2}{c^4} = \frac{1}{6\pi}\frac{1}{\varepsilon_r^{3/2}}\frac{a_H^{5/2}t}{l^2w^{3/2}} = 0.039\end{aligned} \tag{5}$$

Calculation of the dissipation factor and the kinetic inductance factor for a slab-wire pair made of graphene needs special consideration because of the two-dimensional nature of the current transport. The geometry-dependent terms in $\zeta$ and $\xi$ are calculated in the previous paragraph. The resistivity was obtained using experimental data from Li *et al.*[36]. The real part of the measured surface conductivity of graphene to very good approximation is equal to $\sigma_0 = \pi e^2/(2h) = 6.08 \times 10^{-5}$ S m$^{-1}$. The imaginary part is more than 10 times smaller and, as a consequence, there is significant uncertainty in its measured value. We therefore fitted two Drude functions to the experimental data: (i) the first provides a lower bound to the measured imaginary part of the conductivity and (ii) the other provides an upper bound (Supplementary Fig. 3). Note that these fits are phenomenological and are unrelated to the Drude-like behaviour of the intraband carriers, because the current transport is dominated by interband carriers in the infrared and the visible.

The uncertainty in the imaginary part of the conductivity does not affect the value of the dissipation factor, because

$$\mathrm{Re}(\rho) = \frac{\mathrm{Re}(\sigma)}{\mathrm{Re}(\sigma)^2 + \mathrm{Im}(\sigma)^2} \approx \frac{1}{\mathrm{Re}(\sigma)} \tag{6}$$

However, it does lead to uncertainty in the kinetic inductance factor, indicated by the error bars in Fig. 2c. The fitted Drude functions are finally used in equations (4) to determine the dissipation factor and the kinetic inductance factors, respectively.

The properties of an SPP ($\sim\exp[\mathrm{i}(\beta z - \omega t)]$) propagating in the $z$-direction on graphene (dispersion relation in Supplementary Fig. 4a, lateral confinement length in Supplementary Fig. 4b, and propagation length in Fig. 3) were calculated from the dispersion relation derived in ref. 20,

$$\beta = \frac{\omega}{c}\sqrt{1 - \left(\frac{1}{\eta_0\sigma_{||}}\right)^2} \tag{7}$$

where $\eta_0$ is the characteristic impedance of free space. The SPP wavelength is obtained from $\lambda_{SPP} = 2\pi/|\mathrm{Re}(\beta)|$, the propagation length by $1/|\mathrm{Im}(\beta)|$, and the lateral decay length by $1/\mathrm{Re}[\sqrt{(\beta^2 - (\omega/c)^2)}]$. For the conductivity of graphene, $\sigma_{\parallel}$, we used experimental data for strongly biased ($V_{bias} = 71$ V) graphene from ref. 36. In addition, we have used the theoretical model by Peres *et al.* for the conductivity of graphene to calculate the propagation length of a very clean graphene sample[42]. This theoretical data ignores extrinsic scattering such as impurities (which could potentially be removed in cleaner samples), but does account for electron–electron interactions (an intrinsic effect that cannot be removed).

The comparative analysis of metals and conductive oxides in Fig. 5 is based on experimental data from several sources. In Supplementary Table 1, we list the plasma frequency, the collision frequency and the resistivity of the metals and the conducting oxides contained in Fig. 5. References for the experimental data points are also provided in Supplementary Table 1.

Received 16 August 2011; accepted 24 January 2012; published online 4 March 2012

## References


1. Smith, D. R., Pendry, J. B. & Wiltshire, M. C. K. Metamaterials and negative refractive index. *Science* **305,** 788–792 (2004).
2. Shalaev, V. M. Optical negative-index metamaterials. *Nature Photon.* **1,** 41–48 (2006).
3. Soukoulis, C. M. & Wegener, M. Optical metamaterials—more bulky and less lossy. *Science* **330,** 1633–1634 (2010).
4. Yen, T. J. *et al.* Terahertz magnetic response from artificial materials. *Science* **303,** 1494–1496 (2004).
5. Linden, S. *et al.* Magnetic response of metamaterials at 100 terahertz. *Science* **306,** 1351–1353 (2004).
6. Enkrich, C. *et al.* Magnetic metamaterials at telecommunication and visible frequencies. *Phys. Rev. Lett.* **95,** 203901 (2005).
7. Shelby, R. A., Smith, D. R. & Schultz, S. Experimental verification of a negative index of refraction. *Science* **292,** 77–79 (2001).
8. Zhang, S. *et al.* Experimental demonstration of near-infrared negative index metamaterials. *Phys. Rev. Lett.* **95,** 137404 (2005).
9. Shalaev, V. M. *et al.* Negative index of refraction in optical metamaterials. *Opt. Lett.* **30,** 3356–3358 (2005).
10. Plum, E. *et al.* Metamaterial with negative index due to chirality. *Phys. Rev. B* **79,** 035407 (2009).
11. Economou, E. N. Surface plasmons in thin films. *Phys. Rev.* **182,** 539–554 (1969).
12. Boardman, A. D. *Electromagnetic Surface Modes* (Wiley, 1982).
13. Maier, S. A. & Atwater, H. A. Plasmonics: localization and guiding of electromagnetic energy in metal/dielectric structures. *J. Appl. Phys.* **98,** 011101 (2005).
14. Gramotnev, D. K. & Bozhevolnyi, S. I. Plasmonics beyond the diffraction limit. *Nature Photon.* **4,** 83–91 (2010).
15. Catchpole, K. R. & Polman, A. Plasmonic solar cells. *Opt. Express* **16,** 21793–21800 (2008).
16. Soukoulis, C. M., Zhou, J., Koschny, T., Kafesaki, M. & Economou, E. N. The science of negative index materials. *J. Phys. Condens. Matter* **20,** 304217 (2008).
17. Bozhevolnyi, S. I., Volkov, V. S., Devaux, E. & Ebbesen T. W. Channel plasmon-polariton guiding by subwavelength metal grooves. *Phys. Rev. Lett.* **95,** 046802 (2005).
18. Kolomenski, A., Kolomenskii, A., Noel, J., Peng, S. & Schuessler, H. Propagation length of surface plasmons in a metal film with roughness. *Appl. Opt.* **48,** 5683–5691 (2009).
19. Boltasseva, A. & Atwater, H. A. Low-loss plasmonic metamaterials. *Science* **331,** 290–291 (2011).
20. Vakil, A. & Engheta, N. Transformation optics using graphene. *Science* **332,** 1291–1294 (2011).
21. Koppens, F. H. L., Chang, D. E. & García de Abajo, F. J. Graphene plasmonics: a platform for strong light–matter interactions. *Nano Lett.* **11,** 3370–3377 (2011).
22. Chen, H.-T. *et al.* Tuning the resonance in high-temperature superconducting terahertz metamaterials. *Phys. Rev. Lett.* **105,** 247402 (2010).
23. Pendry, J. B., Holden, A. J., Robbins, D. J. & Stewart, W. J. Magnetism from conductors and enhanced nonlinear phenomena. *IEEE Trans. Microwave Theory Tech.* **47,** 2075–2084 (1999).
24. Gorkunov, M., Lapine, M., Shamonina, E. & Ringhofer, K. H. Effective magnetic properties of a composite material with circular conductive elements. *Eur. Phys. J. B* **28,** 263–269 (2002).
25. Engheta, N. Circuits with light at nanoscales: optical nanocircuits inspired by metamaterials. *Science* **317,** 1698–1702 (2007).
26. Koschny, T., Kafeski, M., Economou, E. N. & Soukoulis, C. M. Effective medium theory of left-handed materials. *Phys. Rev. Lett.* **93,** 107402 (2004).
27. Zhang, S., Genov, D. A., Wang, Y., Liu, M. & Zhang, X. Plasmon-induced transparency in metamaterials. *Phys. Rev. Lett.* **101,** 047401 (2008).
28. Papasimakis, N., Fedotov, V. A., Zheludev, N. I. & Prosvirnin, S. L. Metamaterial analog of electromagnetically induced transparency. *Phys. Rev. Lett.* **101,** 253903 (2008).
29. Tassin, P., Zhang, L., Koschny, Th., Economou, E. N. & Soukoulis, C. M. Low-loss metamaterials based on classical electromagnetically induced transparency. *Phys. Rev. Lett.* **102,** 053901 (2009).
30. Liu, N. *et al.* Plasmonic analogue of electromagnetically induced transparency at the Drude damping limit. *Nature Mater.* **8,** 758–762 (2009).
31. Penciu, R. S., Kafesaki, M., Koschny, Th., Economou, E. N. & Soukoulis, C. M. Magnetic response of nanoscale left-handed metamaterials. *Phys. Rev. B* **81,** 235111 (2010).
32. Luan, P. Power loss and electromagnetic energy density in a dispersive metamaterial medium. *Phys. Rev. B* **80,** 046601 (2009).
33. Zhou, J. *et al.* Saturation of the magnetic response of split-ring resonators at optical frequencies. *Phys. Rev. Lett.* **95,** 223902 (2005).
34. Castro Neto, A. H., Guinea, F., Peres, N. M. R., Novoselov, K. S. & Geim, A. K., The electronic properties of graphene. *Rev. Mod. Phys.* **81,** 109–162 (2009).
35. Bonaccorso, F., Sun, Z., Hasan, T. & Ferrari, A. C. Graphene photonics and optoelectronics. *Nature Photon.* **4,** 611–622 (2010).
36. Li, Z. Q. *et al.* Dirac charge dynamics in graphene by infrared spectroscopy. *Nature Phys.* **4,** 532–535 (2008).
37. Horng, J. *et al.*, Drude conductivity of Dirac fermions in graphene. *Phys. Rev. B* **83,** 165113 (2011).
38. Nair, R. R. *et al.* Fine structure constant defines visual transparency of graphene. *Science* **320,** 1308–1308 (2008).
39. Papasimakis, N. *et al.* Graphene in a photonic metamaterial. *Opt. Express* **18,** 8353–8358 (2010).
40. Hanson, G. W. Dyadic Green's functions and guided surface waves for a surface conductivity model of graphene. *J. Appl. Phys.* **103,** 064302 (2008).
41. Jablan, M., Buljan, H. & Soljacic, M. Plasmonics in graphene at infrared frequencies. *Phys. Rev. B* **80,** 245435 (2009).
42. Peres, N. M. R., Ribeiro, R. M. & Castro Neto, A. H. Excitonic effects in the optical conductivity of gated graphene. *Phys. Rev. Lett.* **105,** 055501 (2010).
43. Grushin, A. G., Valenzuela, B. & Vozmediano, M. A. H. Effect of Coulomb interactions on the optical properties of doped graphene. *Phys. Rev. B* **80,** 155417 (2009).
44. Anlage, S. M. The physics and applications of superconducting metamaterials. *J. Opt.* **13,** 024001 (2011).
45. Ordal, M. A., Bell, R. J., Alexander, R. W., Long, L. L. & Querry, M. R. Optical properties of fourteen metals in the infrared and far infrared: Al, Co, Cu, Au, Fe, Pb, Mo, Ni, Pd, Pt, Ag, Ti, V, and W. *Appl. Opt.* **24,** 4493–4499 (1985).
46. Kumar, A. R. *et al.* Far-infrared transmittance and reflectance of $YBa_2Cu_3O_{7-\delta}$ films on Si substrates. *J. Heat Transfer* **121,** 844–851 (1999).
47. Khurgin, J. B. & Sun, G., Scaling of losses with size and wavelength in nanoplasmonics and metamaterials. *Appl. Phys. Lett.* **99,** 211106 (2011).
48. Blaber, M. G., Arnold, M. D. & Ford, M. J. Designing materials for plasmonic systems: the alkali-noble intermetallics. *J. Phys. Condens. Matter* **22,** 095501 (2010).
49. Bobb, D. A. *et al.* Engineering of low-loss metal for nanoplasmonic and metamaterials applications. *Appl. Phys. Lett.* **95,** 151102 (2009).


## Acknowledgements

Work at Ames Laboratory was partially supported by the US Department of Energy, Office of Basic Energy Science, Division of Materials Sciences and Engineering (Ames Laboratory is operated for the US Department of Energy by Iowa State University under contract no. DE-AC02-07CH11358) (theoretical studies) and by the US Office of Naval Research (award no. N00014-10-1-0925, study of graphene). Work at FORTH was supported by the European Community's FP7 projects NIMNIL (grant agreement no. 228637, graphene) and ENSEMBLE (grant agreement no. 213669, study of oxides). P.T. acknowledges a fellowship from the Belgian American Educational Foundation.

## Author contributions

P.T., T.K. and C.M.S. conceived the strategy of comparing conducting materials for metamaterials and plasmonics. P.T. assembled input data and P.T and T. K. performed the calculations. All authors were involved in interpretation of the results. P.T. wrote the paper and all authors commented on the manuscript at all stages.

## Additional information

The authors declare no competing financial interests. Supplementary information accompanies this paper at www.nature.com/naturephotonics. Reprints and permission information is available online at http://www.nature.com/reprints. Correspondence and requests for materials should be addressed to P.T.

nature photonics

SUPPLEMENTARY INFORMATION

DOI: 10.1038/NPHOTON.2012.27

# A comparison of graphene, superconductors and metals as conductors for metamaterials and plasmonics

**Philippe Tassin[1*], Thomas Koschny[1], Maria Kafesaki[2] and Costas M. Soukoulis[1,2]**

[1] Ames Laboratory—U.S. DOE and Department of Physics and Astronomy, Iowa State University, Ames, IA 50011, USA

[2] Institute of Electronic Structure and Lasers (IESL), FORTH, 71110 Heraklion, Crete, Greece

[*] e-mail: tassin@ameslab.gov

## Supplementary Methods

*Introduction*

The foundation of our classification of materials lies in equation (1) of the main text,

$$\Pi = \frac{P_{\mathrm{diss}}}{P_{\mathrm{inc}}} = 2\pi\left(\frac{a_{\mathrm{k}}}{\lambda_0}\right)\frac{F\tilde{\omega}^4\zeta}{\left[\tilde{\omega}^2\left(1+\xi\right)-1\right]^2+\left(\tilde{\omega}\zeta+\tau\tilde{\omega}^5\right)^2}, \tag{S1}$$

which provides the dissipated power fraction of the metamaterial element. In this section, we derive this expression. We consider metamaterials that consist of conducting elements of subwavelength dimensions. A typical example of such an element is depicted in Supplementary Figure 1 in the form of an SRR for illustrative purposes, but the analysis below does not depend on the exact shape.

*Derivation of the circuit equation*

We start the derivation of the circuit equation from Faraday's law in integral form:

$$\oint \mathbf{E}\cdot\mathrm{d}\mathbf{l} = -\frac{\mathrm{d}}{\mathrm{d}t}\iint \mathbf{B}\cdot\mathrm{d}\mathbf{S}. \tag{S2}$$

We choose the path of the contour integral along an electric field line in the conductor closed by an electric field line in the gap (see Supplementary Figure 1). The left-hand side of the above equation can be readily shown to equal the sum of the voltage across the resistor formed by the metallic element and the voltage across the capacitor formed by the gap:

$$\oint \mathbf{E}\cdot\mathrm{d}\mathbf{l} = RI + \frac{1}{C}\int I\,\mathrm{d}t. \tag{S3}$$

DOI: 10.1038/NPHOTON.2012.27

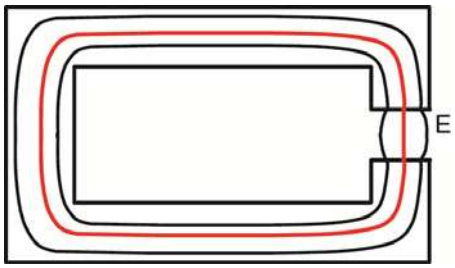


**Supplementary Figure 1 | A quasistatic metallic circuit.** The curved lines are electric field lines along which the contour integral in equation (S2) must be integrated. The field lines follow the current density in the metal and the displacement field in the gap.

The right-hand side of equation (S2) contains a contribution from the incident field as well as a contribution from the magnetic field generated by the current in the circuit:

$$-\frac{\mathrm{d}}{\mathrm{d}t}\iint \mathbf{B}\cdot\mathrm{d}\mathbf{S} = -\frac{\mathrm{d}}{\mathrm{d}t}\iint \mathbf{B}_{\mathrm{inc}}\cdot\mathrm{d}\mathbf{S} - \frac{\mathrm{d}}{\mathrm{d}t}\iint \mathbf{B}_{\mathrm{circuit}}\cdot\mathrm{d}\mathbf{S}. \tag{S4}$$

Because the circuit is smaller than the wavelength, we can assume the incident magnetic field is constant over the circuit, such that the contribution from the incident field equals

$$-\frac{\mathrm{d}}{\mathrm{d}t}\iint \mathbf{B}_{\mathrm{inc}}\cdot\mathrm{d}\mathbf{S} = -\frac{\mathrm{d}}{\mathrm{d}t}\left(\mu_0 H_0 A\cos(\omega t)\right), \tag{S5}$$

where $A$ is the area enclosed by the circuit and $H_0$ is the magnetic field amplitude of the incident wave.

What remains is the contribution from the magnetic induction field generated by the current in the circuit. Again in the quasistatic approximation and after a second differentiation with respect to time, this leads to the circuit equation with the self-inductance term:

$$L\frac{\mathrm{d}^2 I}{\mathrm{d}t^2} + R\frac{\mathrm{d}I}{\mathrm{d}t} + \frac{1}{C}I = -\frac{\mathrm{d}\mathcal{E}}{\mathrm{d}t} = -\frac{\mathrm{d}^2}{\mathrm{d}t^2}\left(\mu_0 H_0 A\cos(\omega t)\right). \tag{S6}$$

This is Kirchoff's equation describing the electrical current, $I$, flowing in the metallic circuit of each meta-atom, driven by the external time-dependent magnetic field of an incident electromagnetic wave. $A$ is the area enclosed by the circuit, $H_0$ the magnetic field amplitude of the incident wave, and $\omega$ the frequency of the incident wave. The inductance, $L$, and capacitance, $C$, must be interpreted as effective values that encompass coupling between neighbouring circuits[24]. The right-hand term in equation (S6) is of course nothing else than the electromotive force, $\mathcal{E}$, induced in the circuit by the incident field. Solving this equation yields a Lorentzian response function with a resonance at frequency $\omega_0 = 1/\sqrt{LC}$ and damping factor $\gamma = R/L$. If we now make the circuit from a conductive material with increasingly high conductivity, the resistance, $R$, becomes smaller and the damping factor goes to zero. The consequence is that the dissipated power at the resonance frequency becomes arbitrarily large, even larger than the power in the incident plane wave, which is clearly unphysical.

The reason behind this "dissipated power catastrophe" is that equation (S6) neglects that the circuit radiates energy away. The radiated power imposes a finite broadening of the resonance—even if the conducting material becomes (almost) lossless. To include radiation effects, we have to take a second look at the contribution of the circuit current to the electromotive force.

To that purpose, we start from the vector potential, **A**, which takes the following form in the Lorentz gauge[S1]:

$$\mathbf{A}(\mathbf{r},t)=\frac{\mu_0}{4\pi}\iiint \mathrm{d}^3\mathbf{r}'\int \mathrm{d}t'\frac{\mathbf{J}(\mathbf{r}',t-|\mathbf{r}-\mathbf{r}'|/c)}{|\mathbf{r}-\mathbf{r}'|}. \tag{S7}$$

Converting to the frequency domain, the vector potential takes the form

$$\mathbf{A}(\mathbf{r})=\frac{\mu_0}{4\pi}\iiint \mathbf{J}(\mathbf{r}')\frac{e^{\mathrm{i}k_0|\mathbf{r}-\mathbf{r}'|}}{|\mathbf{r}-\mathbf{r}'|}\mathrm{d}^3\mathbf{r}', \tag{S8}$$

where $k_0 = \omega/c$ is the free-space wave number and $c$ is the speed of light in vacuum. The integral is over all currents, i.e., over the conducting medium. The magnetic induction field generated by the circuit currents can be obtained from $\mathbf{B}=\nabla\times\mathbf{A}$:

$$-\quad \mathbf{B}(\mathbf{r})=\frac{\mu_0}{4\pi}\iiint \mathbf{J}(\mathbf{r}')\quad\frac{\mathbf{r}-\mathbf{r}'}{|\mathbf{r}-\mathbf{r}'|}\left(\frac{1}{|\mathbf{r}-\mathbf{r}'|}\quad \mathrm{i}k_0\right)\frac{e^{\mathrm{i}k_0|\mathbf{r}-\mathbf{r}'|}}{|\mathbf{r}-\mathbf{r}'|}\mathrm{d}^3\mathbf{r}'. \tag{S9}$$

Since the conducting element is of subwavelength dimensions, all currents in the circuit are confined in a region sufficiently smaller than a wavelength, i.e. $|\mathbf{r}-\mathbf{r}'|\ll 2\pi/k_0$. This allows approximating the exponential function in equation (S9) by the first terms of its Taylor expansion in i$k_0$. The lowest-order term yields

$$-\ \mathbf{B}^{(0)}(\mathbf{r})=\frac{\mu_0}{4\pi}\iiint \mathbf{J}(\mathbf{r}')\quad\frac{\mathbf{r}-\mathbf{r}'}{|\mathbf{r}-\mathbf{r}'|^3}\mathrm{d}^3\mathbf{r}'. \tag{S10}$$

This is Biot-Savart's expression for the quasistatic field solution. It gives rise to the self-inductance term in the circuit equation and Neumann's formula for the self-inductance[S2]. The higher-order terms in $(\mathrm{i}k_0)^m$ are

$$\mathbf{B}^{(m)}(\mathbf{r})=\left(\mathrm{i}k_0\right)^m\frac{m-1}{m!}\frac{\mu_0}{4\pi}\iiint \mathrm{d}^3\mathbf{r}'\mathbf{J}(\mathbf{r}')\times\frac{\mathbf{r}-\mathbf{r}'}{|\mathbf{r}-\mathbf{r}'|}|\mathbf{r}-\mathbf{r}'|^{m-2}. \tag{S11}$$

The first-order term ($m=1$) vanishes. The second-order term ($m=2$) is an imaginary number and, thus, results in a reactive contribution to the impedance of the circuit. It will merely alter the resonance frequency of the circuit slightly. The third-order term is real and results in a resistive contribution to the impedance of the circuit. This is the term we need. In a sufficiently lossy circuit, this term can be neglected with respect to the voltage across the conductor. However, if we let the resistivity of the conducting medium become sufficiently small, the $m=3$ term must be taken into consideration, since it becomes the leading term in the resistive part of the circuit impedance.

DOI: 10.1038/NPHOTON.2012.27

The third-order term yields

$$\mathbf{B}^{(3)}(\mathbf{r}) = -\left(\mathrm{i}k_0\right)^3 \frac{\mu_0}{12\pi} \iiint \mathbf{J}(\mathbf{r}') \quad (\mathbf{r} \quad \mathbf{r}') \mathrm{d}^3\mathbf{r}' \\ = \mathrm{i}k_0^3 \frac{\mu_0}{6\pi} \mathbf{m}, \tag{S12}$$

with $\mathbf{m}$ the magnetic dipole moment of the circuit, and the electromotive force generated by this field becomes

$$-\frac{\mathrm{d}}{\mathrm{d}t} \iint \mathbf{B}^{(3)} \cdot d\mathbf{S} = \mathrm{i}\omega \iint \mathrm{i}k_0^3 \frac{\mu_0}{6\pi} \mathbf{m} \cdot d\mathbf{S} = -\frac{\mu_0 \omega^4 A^2}{6\pi c^3} I, \tag{S13}$$

where $A$ is the area enclosed by the circuit. With this additional term, we arrive at the circuit equation that includes the effects of the radiation reaction on the circuit:

$$L\frac{\mathrm{d}^2 I}{\mathrm{d}t^2} + \left(R + R_{\mathrm{rad}}\right)\frac{\mathrm{d}I}{\mathrm{d}t} + \frac{1}{C} I = -\frac{\mathrm{d}\mathcal{E}}{\mathrm{d}t} = -\frac{\mathrm{d}^2}{\mathrm{d}t^2}\left(\mu_0 H_0 A \cos(\omega t)\right), \tag{S14}$$

where the radiation resistance is given by

$$R_{\mathrm{rad}} = \frac{\mu_0 \omega^4 A^2}{6\pi c^3}. \tag{S15}$$

One can verify that this expression for the radiation resistance is the same as the radiation resistance of a subwavelength antenna as determined from the radiated power in the far-field zone[S1].

We have omitted here the magnetic fields from neighbouring circuits in the metamaterial. These neighbouring circuits will have mainly two consequences: there will be mutual coupling between the magnetic fields and there may be local field effects. Both effects have been studied by Gorkunov *et al.*[24], who show they lead to (i) a renormalization of the circuit parameters and (ii) the emergence of a Clausius-Mosotti functional form of the permeability. The result is that the resonance slightly differs from the Lorentzian shape and that the resonance frequency shifts somewhat. We can neglect these effects here in our comparison of conducting materials, because they are material-independent and will not affect the relative difference between materials.

*Derivation of the magnetic susceptibility and the dissipated power*

The circuit equation can be most easily solved in the frequency domain:

$$\left(-\mathrm{i}\omega L + \left(R + R_{\mathrm{rad}}\right) - \frac{1}{\mathrm{i}\omega C}\right) I = \mathrm{i}\omega A \mu_0 H_0. \tag{S16}$$

Solving this equation for the induced current in the circuit yields

$$I = -\frac{\omega^2 A\mu_0 H_0 / L}{\omega^2 + \mathrm{i}\omega\left(\frac{R+R_{\mathrm{rad}}}{L}\right) - \frac{1}{LC}} = -\frac{\omega^2 A\mu_0 H_0 / L}{\omega^2 + \mathrm{i}\omega\left(\frac{R+R_{\mathrm{rad}}}{L}\right) - \omega_0^2}. \tag{S17}$$

Each circuit has a magnetic dipole moment $m = A \times I$, and a metamaterial with $N$ circuits per unit volume ($N = 1/V_{\mathrm{uc}}$, where $V_{\mathrm{uc}}$ is the volume of a unit cell) has therefore a susceptibility of

$$\chi = -\frac{\omega^2 \mu_0 A^2 N / L}{\omega^2 + \mathrm{i}\omega\left(\frac{R+R_{\mathrm{rad}}}{L}\right) - \omega_0^2}. \tag{S18}$$

Introducing the filling factor

$$F = \mu_0 A^2 N / L, \tag{S19}$$

the susceptibility can be cast in the more customary form

$$\chi = -\frac{F\omega^2}{\omega^2 + \mathrm{i}\omega\left(\frac{R+R_{\mathrm{rad}}}{L}\right) - \omega_0^2}. \tag{S20}$$

The power dissipated by a single circuit can be found from the Ohmic heat formula:

$$P_{\mathrm{diss}} = \frac{1}{2}\mathrm{Re}(R)|I|^2 = \frac{1}{2}\frac{\omega^4 A^2 \mu_0^2 H_0^2 \,\mathrm{Re}(R) / L^2}{\left(\omega^2 - \omega_0^2\right)^2 + \omega^2\left(\frac{R+R_{\mathrm{rad}}}{L}\right)^2}. \tag{S21}$$

Note, the dissipated power function broadens by the radiation resistance, but the radiated power itself is not a dissipation loss—it is, in fact, a much desired effect, since the radiated waves of all the circuits eventually combine to form the electromagnetic waves of the negative-permeability metamaterial. The optical power of the incident wave per unit cell equals

$$P_{\mathrm{inc}} = \frac{1}{2}E_0 H_0 a_{\mathrm{E}} a_{\mathrm{H}} = \frac{1}{2}\mu_0 H_0^2 \frac{c}{N a_{\mathrm{k}}}, \tag{S22}$$

where $a_{\mathrm{E}}$, $a_{\mathrm{H}}$, and $a_{\mathrm{k}}$ are the lattice constants along the electric field, the magnetic field, and the wave vector of the incident wave, respectively.

DOI: 10.1038/NPHOTON.2012.27

Combining equations (S21) and (S22), we eventually find the ratio of the dissipated power to the incident power:

$$\Pi = \frac{P_{\mathrm{diss}}}{P_{\mathrm{inc}}} = \frac{a_{\mathrm{k}}}{c}\frac{\mathrm{Re}(R)}{L}\frac{F\omega^4}{\left(\omega^2-\omega_0^2\right)^2+\omega^2\left(\frac{R+R_{\mathrm{rad}}}{L}\right)^2}. \tag{S23}$$

*Introduce dimensionless frequency*

Finally, we introduce dimensionless variables to make the expressions independent of the frequency band of interest. This is achieved by normalizing the frequency to the geometric resonance frequency:

$$\tilde{\omega} = \frac{\omega}{\omega_0}. \tag{S24}$$

In this way, the susceptibility can be written as

$$\chi = -\frac{F\tilde{\omega}^2}{\tilde{\omega}^2 - 1 + \mathrm{i}\tilde{\omega}\left(\frac{R+R_{\mathrm{rad}}}{\sqrt{L/C}}\right)}, \tag{S25}$$

and the dissipated power fraction as

$$\Pi = \frac{P_{\mathrm{diss}}}{P_{\mathrm{inc}}} = 2\pi\left(\frac{a_{\mathrm{k}}}{\lambda_0}\right)\frac{\mathrm{Re}(R)}{\sqrt{L/C}}\frac{F\tilde{\omega}^4}{\left(\tilde{\omega}^2-1\right)^2+\tilde{\omega}^2\left(\frac{R+R_{\mathrm{rad}}}{\sqrt{L/C}}\right)^2}. \tag{S26}$$

*Introduce the dimensionless variables ζ, ξ, and β*

At finite frequencies, the resistivity and, hence, the resistance, $R$, are complex quantities, due to the finite mass of the charge carriers. Therefore, we define two variables, for the real and the imaginary part of the resistance, respectively:

- Dissipation factor:

$$\varsigma = \frac{\mathrm{Re}(R)}{\sqrt{L/C}} \tag{S27}$$

- Kinetic inductance factor:

$$\xi = -\frac{\mathrm{Im}(R)}{\tilde{\omega}\sqrt{L/C}} \tag{S28}$$

- Radiation loss parameter:

$$\tau\tilde{\omega}^4 = \frac{R_{\mathrm{rad}}}{\sqrt{L/C}} = \frac{\mu_0\omega^4A^2}{6\pi c^3\sqrt{L/C}} \quad \frac{1}{6\pi}\frac{\sqrt{\mu_0/\varepsilon_0}}{\sqrt{L/C}}\frac{\omega_0^4A^2}{c^4}\tilde{\omega}^4 \tag{S29}$$

In terms of these dimensionless parameters, the susceptibility and dissipated power loss fraction are

$$\chi = -\frac{F\tilde{\omega}^2}{\tilde{\omega}^2\left(1+\xi\right)-1+\mathrm{i}\left(\tilde{\omega}\zeta+\tau\tilde{\omega}^5\right)} \tag{S30}$$

and

$$\Pi = \frac{P_{\mathrm{diss}}}{P_{\mathrm{inc}}} = 2\pi\left(\frac{a_{\mathrm{k}}}{\lambda_0}\right)\frac{F\tilde{\omega}^4\zeta}{\left[\tilde{\omega}^2\left(1+\xi\right)-1\right]^2+\left(\tilde{\omega}\zeta+\tau\tilde{\omega}^5\right)^2} \quad \text{equation (1)} \tag{S31}$$

The dissipation factor $\zeta$ is a dimensionless quantity determining the dissipative loss. This is discussed in the main text (figure 1) and forms the basis for our classification of conducting materials for use in resonant metamaterials.

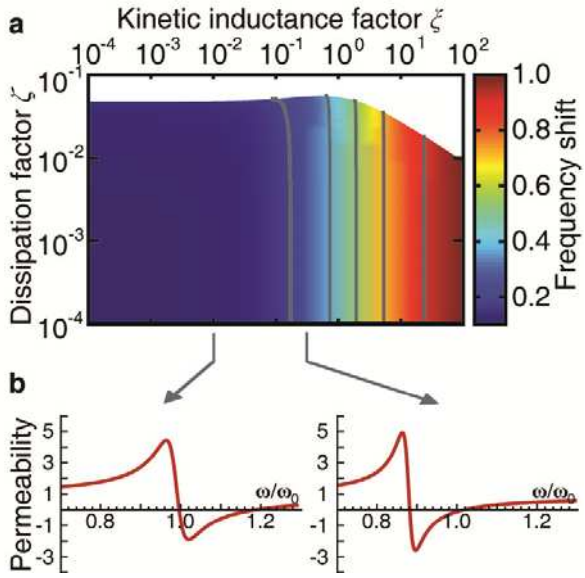


**Supplementary Figure 2 | Frequency redshift in a metamaterial with $F$ = 0.37 and $\tau$ = 0.039; quantities are calculated for the slab-wire pair of figure 2a. a,** Contour plot indicating how much the frequency at which $\mu(\omega) = -1$ is redshifted due to the kinetic inductance effect and the dissipation factor. The contour lines are approximately vertical, signifying that the resonance frequency depends only on the kinetic inductance factor to good approximation. The white region is the cut-off region where the resonance is too shallow to obtain negative permeability $\mu(\omega) = -1$. **b,** Resonance shapes of the magnetic permeability for kinetic inductance factors $\xi$ = 0.01 and $\xi$ = 0.3. The dissipation factor was taken as $\zeta$ = 0.02. The strength of the resonance is almost unaltered by the kinetic inductance.

The kinetic inductance factor determines the saturation of the resonance frequency of negative-permeability metamaterials when they are scaled down towards optical frequencies[33,31]. This effect is due to the contribution of the kinetic inductance of the free electrons or, in other words, to the mass inertia of the charge carriers. This is a material

DOI: 10.1038/NPHOTON.2012.27

effect and should be reflected in our model. To this end, we plot in Supplementary Figure 2a the frequency at which the desired magnetic permeability ($\mu = -1$) is realized as a function of the parameters $\zeta$ and $\xi$. First, the plot reveals that the frequency is essentially independent of the dissipation factor $\zeta$. When the kinetic inductance factor is small, the resonance occurs at approximately $\omega = \omega_0$ and the frequency at which $\mu = -1$ is slightly larger. If the kinetic inductance factor is increased to a value of the order of unity, the resonance frequency is moved to smaller values (and the width of the negative permeability band decreases). This effect is confirmed by the permeability graphs in Supplementary Figure 2b.

## Supplementary Figures and Table

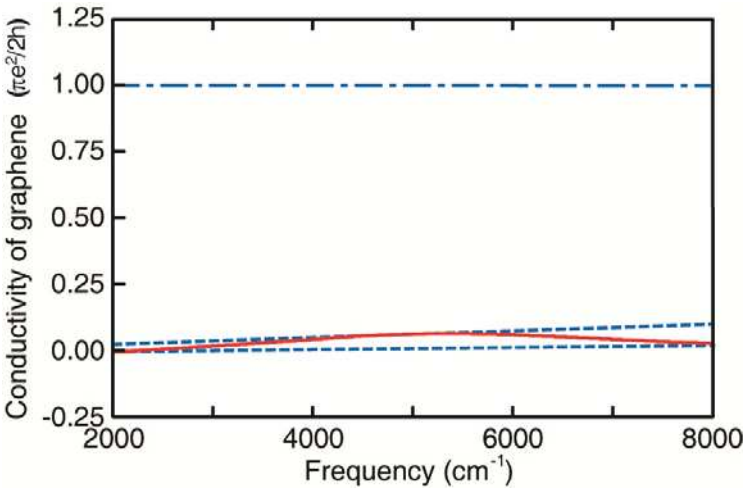


**Supplementary Figure 3 | Surface conductivity of charge-neutral graphene from reference 36.** Blue, dash-dotted line: real part of the surface conductivity (measured and fitted curves coincide). Red line: measured imaginary part of the surface conductivity. Blue, dashed lines: fitted curves representing an upper and lower bound to the measured data for the imaginary part of the surface conductivity.

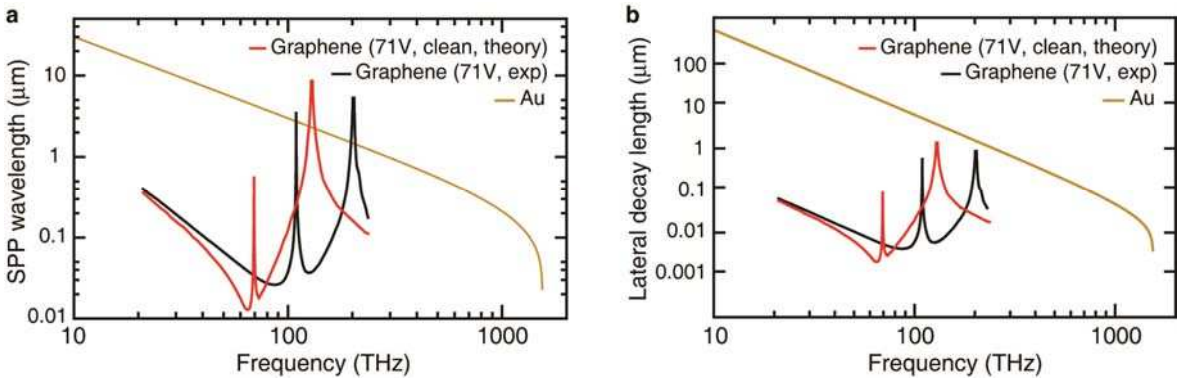


**Supplementary Figure 4 | Surface plasmon polaritons on graphene and gold.** The results for gold are for a 30 nm thick film at room temperature. The results for graphene are for strongly biased graphene calculated from experimental conductivity data (from ref. 36) and calculated from theoretical conductivity data that incorporates electron-electron interactions (from ref. 42). **a**, The wavelength of a surface plasmon polariton on graphene. Around 30 THz, the wavelength of SPPs on graphene is much smaller than the free-space wavelength $\lambda_0 = 2\pi c/\omega$. This is an immediate consequence of the large kinetic inductance of graphene as quantified by the kinetic inductance factor shown in figure 2c. **b**, Lateral confinement (away from the surface) of surface plasmon polaritons. The high kinetic inductance of graphene results in very good confinement with sub-micrometer decay length at mid-infrared frequencies.

DOI: 10.1038/NPHOTON.2012.27

**Supplementary Table 1 | Plasma frequency, collision frequency, and resistivity of the metals and conducting oxides shown in figure 5.** The numbers between parentheses refer to the literature where the data were obtained from; the quantities without references have been derived by us. We note again that the collision frequency includes all possible scattering mechanisms and is therefore frequency-dependent. The following labels are used to indicate the frequency/wavelength at which the data are evaluated: GHz (1 GHz), IR (1.55 μm), and VIS (500 nm).

| | $\omega_p$ (Trad/s) | Γ (THz) | Re(ρ) (Ωm) |
|---|---|---|---|
| **Ag (GHz)** | 13634 (S3) | 26.6 | 1.62E-08 (S4) |
| **Ag (IR)** | 13634 (S3) | 28.8 | 1.75E-08 (S5) |
| **Ag (VIS)** | 13634 (S3) | 131 | 7.99E-08 (S5) |
| **Al (GHz)** | 24001 (S3) | 138 | 2.71E-08 (S6) |
| **Al (IR)** | 24001 (S3) | 321 | 6.30E-08 (S5) |
| **Al (VIS)** | 24001 (S3) | 930 | 1.82E-07 (S5) |
| **Au (GHz)** | 13697 (S3) | 37.5 | 2.26E-08 (S4) |
| **Au (IR, Ordal)** | 13697 (S3) | 81.4 | 4.90E-08 (S6) |
| **Au (IR, J&C)** | 13697 (S3) | 125 | 7.54E-08 (S5) |
| **Au(VIS)** | 13697 (S3) | 7095 | 4.27E-06 (S5) |
| **AZO (GHz)** | 1602 (S7) | 11364 | 5.00E-04 (S8) |
| **Be (GHz)** | 28023 (S3) | 257 | 3.70E-08 (S4) |
| **Cr (GHz)** | 6911 (S9) | 13.2 (S9) | 3.12E-08 |
| **Cr (IR)** | 6911 (S9) | 1087 | 2.57E-06 (S10) |
| **Cr (VIS)** | 6911 (S9) | 403 | 9.53E-07 (S11) |
| **Cu (GHz)** | 16399 (S3) | 40.8 | 1.71E-08 (S4) |
| **Cu (IR)** | 16399 (S3) | 253 | 1.06E-07 (S5) |
| **Cu (VIS)** | 16399 (S3) | 5803 | 2.44E-06 (S5) |
| **ITO (GHz+IR)** | 1602 (S12) | 145 (S12) | 6.37E-06 |
| **K (GHz)** | 5648 (S3) | 20.9 | 7.39E-08 (S4) |
| **K(IR)** | 5648 (S3) | 29.1 | 1.03E-07 (S11) |
| **K(VIS)** | 5648 (S3) | 145 | 5.15E-07 (S11) |
| **KAu (GHz)** | 2339 (S13) | 34.0 | 7.01E-07 (S13) |
| **KAu (IR)** | 2339 (S13) | 36.0 | 7.42E-07 (S13) |
| **KAu (VIS)** | 2339 (S13) | 84.8 | 1.75E-06 (S13) |

**Supplementary Table 1** | Continued.

| | $\omega_p$ (Trad/s) | Γ (THz) | Re(ρ) (Ωm) |
|---|---|---|---|
| **Li (GHz)** | 9738 (S14) | 79.5 | 9.47E-08 (S4) |
| **Li (IR)** | 9738 (S14) | 209 | 2.49E-07 (S11) |
| **Li (VIS)** | 9738 (S14) | 691 | 8.23E-07 (S11) |
| **LiAg (GHz)** | 11060 (S13) | 82.1 | 7.58E-08 (S13) |
| **LiAg (IR)** | 11060 (S13) | 438 | 4.04E-07 (S13) |
| **LiAg (VIS)** | 11060 (S13) | 764 | 7.05E-07 (S13) |
| **Na (GHz)** | 8168 (S15) | 28.8 | 4.88E-08 (S4) |
| **Na (IR)** | 8168 (S15) | 50.1 | 8.48E-08 (S13) |
| **Na (VIS)** | 8168 (S15) | 174 | 2.94E-07 (S13) |
| **Pd (GHz)** | 8293 (S6) | 65.4 | 1.07E-07 (S4) |
| **Pt** | 7791 (S6) | 56.0 (S6) | 1.04E-07 |
| **ZrN (IR)** | 11812 (S16) | 70.3 (S16) | 5.69E-08 |

DOI: 10.1038/NPHOTON.2012.27

## References


S1. Jackson, J. D. *Classical Electromagnetism* (Wiley, New York, 1962).

S2. Reitz, J. R. & Milford, F. J. *Foundations of Electromagnetic Theory, 2nd Edition* (Addison-Wesley, Reading, 1967).

S3. Fox, M. *Optical Properties of Solids* (Oxford Univ. Press, Oxford, 2001).

S4. Haynes, W. M. *CRC Handbook of Chemistry and Physics, 92nd Edition* (CRC Press, Boca Raton, 2011).

S5. Johnson, P. B. & Christy, R. W. Optical constants of the noble metals. *Phys. Rev. B* **6**, 4370-4379 (1972).

S6. Ordal, M. A. & Bell, R. J., Alexander, R. W., Long, L. L. & Querry, M. R. Optical properties of fourteen metals in the infrared and far infrared: Al, Co, Cu, Au, Fe, Pb, Mo, Ni, Pd, Pt, Ag, Ti, V, and W. *Appl. Opt.* **24**, 4493-4499 (1985).

S7. Rhodes, C. L. *et al.* Characterization of Monolayer Formation on Aluminum-Doped Zinc Oxide Thin Films. *Langmuir* **24**, 433-440 (2008).

S8. Galca, A. C., Secu, M., Vlad, A. & Pedarnig, J. D. Optical properties of zinc oxide thin films doped with aluminum and lithium. *Thin Solid Films* **518**, 4603-4606 (2010).

S9. Lovrincic, R. & Pucci, A. Infrared optical properties of chromium nanoscale films with a phase transition. *Phys. Rev. B* **80**, 205404 (2009).

S10. Bos, L. W. & Lynch, D. W. Optical properties of antiferromagnetic chromium and dilute Cr-Mn and Cr-Re alloys. *Phys. Rev. B* **2**, 4567-4577 (1970).

S11. Lynch, D. W. & Hunter, W. R. in *Handbook of Optical Constants of Solids II*, E. D. Palik, ed. (Academic Press, San Diego, 1991).

S12. Chen, C.-W. *et al.* Frequency-dependent complex conductivities and dielectric responses of indium tin oxide thin films from the visible to the far-infrared. *IEEE J. Quant. Electron.* **46**, 1746-1754 (2010).

S13. Blaber, M. G., Arnold, M. D. & Ford, M. J. Designing materials for plasmonic systems: the alkali-noble intermetallics. *J. Phys.: Condens. Matter* **22**, 095501 (2010).

S14. Dugdale, J. S., Gugan, D. & Okumura, K. The electrical resistivity of lithium-6. *Proc. R. Soc. Lond.* A **263**, 407-419 (1961).

S15. Kittel, C. *Introduction to Solid State Physics* (Wiley, New York, ed. 17, 1996).

S16. Veszelei, M., Andersson, K., Ribbing, C.-G., Jarrendahl, K. & Arwin, H. Optical constants and Drude analysis of sputtered zirconium nitride films. *Appl. Opt.* **33**, 1993-2001 (1994).